ELSEVIER

Contents lists available at ScienceDirect

Journal of Manufacturing Processes

journal homepage: www.elsevier.com/locate/manpro





Processing aluminum alloy with hybrid wire arc additive manufacturing and ultrasonic nanocrystalline surface modification to improve porosity, surface finish, and hardness

Wei Li ^{a,*}, Auezhan Amanov ^b, Kishore Mysore Nagaraja ^a, Benquan Li ^a, Bharath Bhushan Ravichander ^a, Runyu Zhang ^a, Hongbing Lu ^a, Dong Qian ^a, Golden Kumar ^a, Young Sik Pyun ^b

ARTICLE INFO

Keywords: Wire arc additive manufacturing Ultrasonic nanocrystal surface modification Porosity Surface roughness Hardness

ABSTRACT

In this paper, a novel hybrid wire arc additive manufacturing (WAAM) and ultrasonic nanocrystal surface modification (UNSM) on porosity manipulation and surface properties of aluminum 5356 alloys was studied. The goal is to improve the quality of the WAAM-built part by eliminating bigger pores and reducing its size, reducing surface roughness, and increasing surface hardness. The as-built WAAM and WAAM-UNSM-treated samples were quantitatively studied for porosity using an X-ray micro-computed tomography (μ -CT). The surface roughness was measured on the surface profile of the same samples before and after UNSM treatment. Followed by the Vickers micro-hardness tests to evaluate the hardness modified by the influence of the UNSM treatment. It was found that the bigger pores in the as-built WAAM samples were eliminated and the medium-sized pores were shrunk to almost half the size after the UNSM treatment. Further, the UNSM treatment showed a significant improvement in both surface roughness and hardness on the WAAM Al5356 samples. This experimental work demonstrates the critical advantages of hybrid WAAM-UNSM in improving the qualities of the WAAM processed parts.

1. Introduction

Wire arc additive manufacturing (WAAM) has been considered as a potential solution for fabricating medium-to-large size metallic components with a near-100 % material deposition rate. In the WAAM process (Fig. 1(a)), metallic wire is fed and melted by an electric arc to fabricate a three-dimensional (3D) part in a layer-by-layer fashion. The long reach of the robotic arm and its flexible degree of freedom enables the WAAM to print complex and large metal components. However, WAAM often generates internal pores of various sizes, which are mainly caused by the hydrogen vaporized from the moisture, grease, hydrocarbon contaminants on the wire surface, and the entrapped shielding gas which cannot escape due to the rapid solidification in the WAAM process [1–6].

Porosity is a critical barrier preventing the WAAM technique from wide application [7-13]. The porosities in the Al samples built using the

WAAM process are usually influenced by shielding gas, gas flow rate, meltpool temperature and phase change, and deposition strategy. For example, the size and number of porosities generation can be altered by changing the deposition strategy from hatching to circling conditions. The temperature effect in the meltpool region and the phase change could be the dominant cause of the porosity formation in the WAAM-processed Al samples, and the location could cover the entire cross-section [14]. Furthermore, the bigger pores in the WAAM-processed Al samples could form near the inter-layer of the deposition arbitrarily. Hence, the WAAM-processed Al samples tend to form porosity throughout the deposition region arbitrarily due to various factors. This necessitates the use of post-processing techniques to alleviate these porosities.

To alleviate porosity, the commonly used method is hot isostatic pressing (HIP) in which high temperature and isostatic pressure are applied to compress the metal part to reduce pore volume. However, HIP

E-mail address: Wei.Li@UTDallas.edu (W. Li).

^a Department of Mechanical Engineering, The University of Texas at Dallas, Richardson, TX, USA

b Department of Mechanical Engineering, Sun Moon University, Asan 31460, South Korea

^{*} Corresponding author.

is unable to eliminate pores, and to some extent can promote the regrowth of gas porosities [15,16]. In addition, it is often hard to process large-scale WAAMed parts using HIP due to the process space constraint. Another concern in the WAAM process is the low surface quality which is frequently observed in other metal 3D printing technologies [17,18]. The thermal history of each layer of printed material is not always consistent. It is caused by various WAAM parameters that influence the surface morphology and temperature of the previously printed layer [19]. This lead to WAAMed parts exhibiting a high level of surface roughness that affects corrosion, wear, and fatigue resistances, which are not suitable for direct use without post-treatment surface modification [20,21].

The ultrasonic nanocrystal surface modification (UNSM) [22] is a surface severe plastic deformation (S²PD) technique that has been applied in a wide range of applications [23,24]. In the UNSM (Fig. 1(b)), a tungsten carbide ball tip is attached to an ultrasonic device to generate indentation strikes at 20,000 or more times per second on a cylindrical part rotating at a feed speed V (mm/rev) at the surface subjected to striking. When coupled with translational motion involved in WAAM, this leads to 1000 to 10,000 strikes/mm². The striking tip scans the part surface with a scanning speed S (mm/min). The amplitude and frequency of the striking force (*F*) are controlled by an ultrasonic transducer. The striking force consists of two components, a static load P_{st} and a dynamic load $P(F = P_{st} + P \sin 2\pi f t, f \text{ is the striking frequency})$ [25]. The static and dynamic components of the loads can be independently adjusted with a specific combination, severe plastic deformation and grain refinement can be induced in the near-surface region [26,27]. The UNSM can generate more than 500 µm layer of nanocrystal grains (30-100 nm) and high levels of compressive residual stress from the surface down to the part [28-30]. As shown in Fig. 1(b), due to the plastic deformation, a significantly larger number of pores are compressed and closed by the compacting effect [31-34]. Smoother surfaces and lower subsurface porosity will certainly lead to better mechanical properties in the treated material [35,36]. Compared to other S²PD processes like water jet peening and laser shock peening, UNSM avoids the water medium and the optics, facilitating integration with the WAAM process [37,38].

The hybrid WAAM-UNSM process has multiple benefits. 1) The severe plastic deformation formed in UNSM can reduce the porosity formed in WAAM. 2) It allows for more flexible surface quality control of the WAAMed part by reducing the surface roughness. 3) The hardness of the WAAMed part can be enhanced with the UNSM treatment, so the related mechanical properties and abrasive resistance can be strengthened. 4) The induced compressive residual stress in each layer increases the atomic density of the metal [43], thereby improving the mechanical properties.

This study involves a hybrid WAAM-UNSM integrated process applied on Al5356 samples to quantify porosity, surface roughness, and hardness. The effect of UNSM static and dynamic loads are studied for its influence on the porosity distribution in the Al5356 samples. The

improvement in porosity, surface roughness, and hardness under the influence of the UNSM scanning speed over its different static loads on the WAAMed sample is closely monitored and quantified using μ -CT scanning. This process and methodology are expandable to the successive layers to further develop WAAM-UNSM as an integrated in-situ processing for Aluminum layer-by-layer. The process parameters for WAAM and UNSM were carefully chosen based on the laboratory experience of the authors on metal processing. There are many studies reported in the previous section that identifies critical technology advantages of the UNSM and WAAM processes separately. Since the hybrid WAAM-UNSM is not explored and the current research fills the gap in developing it as an in-situ approach, layer-by-layer during the WAAM process. Further to avoid the use of many input parameters for both WAAM and UNSM as independent parameters and their influence study, this research study considers static load in the UNSM as the main category to study the influence on the WAAMed Al5356 samples. It keeps all other input parameters of WAAM and UNSM the same throughout the sample preparation. The study mainly aims to quantify the improvement of porosity, surface roughness, and hardness under the influence of hybrid WAAM and UNSM processes that can be expandable to develop an integrated process structure for each layer printed.

2. Material and method

The chemical composition of Al5356 alloy is outlined in Table 1. At first, four different Al5356 samples were printed with the same substrate material using the WAAM process. Three of these samples were considered for UNSM treatment, and one is considered an as-built condition for data comparison. Each sample was treated with three striking forces during the UNSM process. Before and after UNSM treatment, these samples were measured for porosity using an X-ray $\mu\text{-CT}$ scanner, surface roughness, and surface hardness using the Vickers hardness tests.

2.1. Experimental platforms

The WAAM platform as shown in Fig. 2 has an ABB programmable robotic arm (Fig. 2(a)) (IRB 140, six degrees of freedom, 810 mm reach) controls the motion of the WAAM process to print 3D parts. The robotic arm is integrated with a Fronius TPS 320i welder (Fig. 2(b)). The wire material used is aluminum 5356 (Al5356) with 0.889mm diameter. Al5356 is a widely used alloy because of its high shear strength, high electrical conductivity, strong corrosion resistance, and good low-temperature properties.

Table 1
Material composition of Al5356 wire (wt%).

Alloy	Si	Fe	Cu	Mn	Mg	Zn	Al
Al5356	0.25	0.4	0.1	0.05-0.2	5.0	0.1	Balance

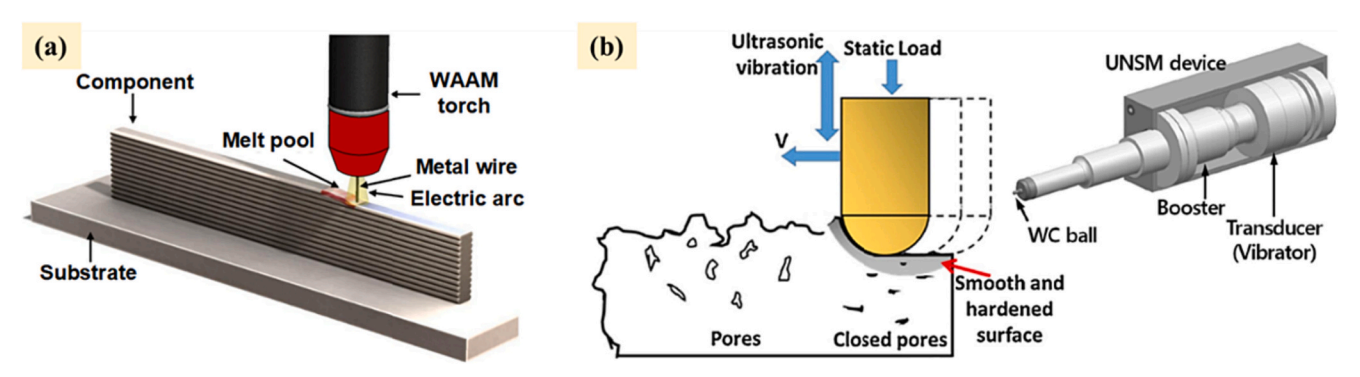


Fig. 1. (a). Wire arc additive manufacturing (WAAM) [39,40]; (b). ultrasonic nanocrystal surface modification (UNSM) [41,42].

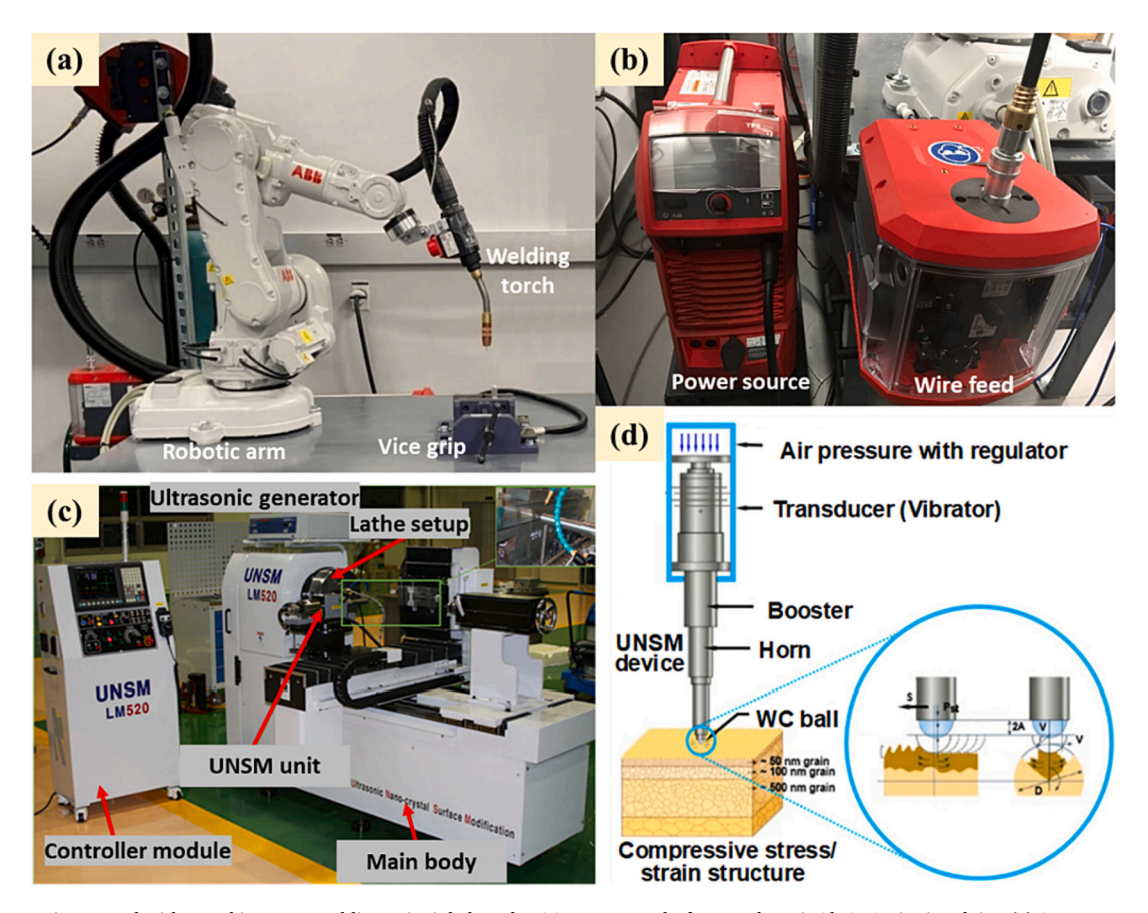


Fig. 2. Robotic arm integrated with metal inert gas welding principle based WAAM process platform to deposit Al5356 wire involving (a) ABB programmable robotic arm (IRB 140, six degrees of freedom, 810 mm reach), (b) WAAM process power source with wire feed. (c) UNSM platform mounted on a lathe setup and its working principle (d) involving WC ball tip causing an S²PD at an ultrasonic frequency.

2.2. Wire arc additive manufacturing of Al5356

The WAAM process parameters considered to print Al5356 are given in Table 2. The printed samples with a print strategy and the sample dimension are shown in Fig. 3. At first, the Al5356 substrate with 38 \times 38 \times 12 mm dimension was fixed onto a bench vice, and the same material in the wire form is fed through a wire feeder with a feeding rate of 595 in/min. The wire serves as both heat source generated by arc at the wire tip with a current of 136 A passed through the power source and as a filler material. An arc between the wire tip and the workpiece melts both to form a deposition pool. A single layer with 12 tracks printed along the $\pm y$ axis with a hatch spacing of 2 mm, as indicated in Fig. 3(a). A total of four samples set printed as shown in Fig. 3(b) to be used for UNSM treatment.

${\it 2.3. \ Ultrasonic \ nanocrystal \ surface \ modification \ of \ Al5356 \ WAAMed \ samples}$

The UNSM platform (see Fig. 2(c)) used in this study was supported

Table 2Printing parameters considered for the WAAM process to print Al5356.

Parameters	Values/units		
Printing voltages	19.8 V		
Printing currents	136 A		
Wire feeding rates	595 in/min		
Hatch space	2 mm		
Tracks number	12		
Traveling speed	20 mm/s		

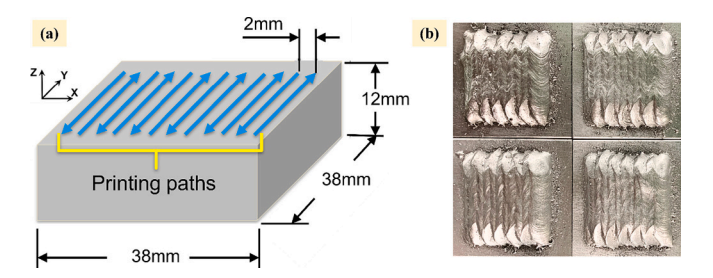


Fig. 3. (a) Al5356 substrate with printing path strategy considered for four Al5356 single layer multi-track samples (b) printed using WAAM process with a hatch spacing between the tracks of 2 mm.

by Sun Moon University (South Korea). This UNSM system (UNSM LM520) is integrated into a lathe platform and has a controller and ultrasonic generator. The LM-520 UNSM platform can induce a dynamic load at 20 kHz with the displacement amplitude of the ultrasonic oscillation of 30 μm . The WC with a 2.4 mm tip (Fig. 2(d)) diameter was used to scan multiple tracks on the surface profile using a square wave with a scanning speed of 1000 mm/min. The area covered under the UNSM treatment was 14 mm \times 14 mm. For the UNSM surface treatment, three different static load cases of 50 N, 80 N, and 100 N were considered. Further, the dynamic load of 20 kHz and scanning speed of 1000 mm/min were kept constant. The first sample was considered an asbuilt condition to compare with three UNSM cases. These samples representing the as-built and after-UNSM treatment are shown in Fig. 4.

The UNSM-processed Al5356 samples possessed smoother surfaces compared to the as-built sample because of severe plastic deformations.

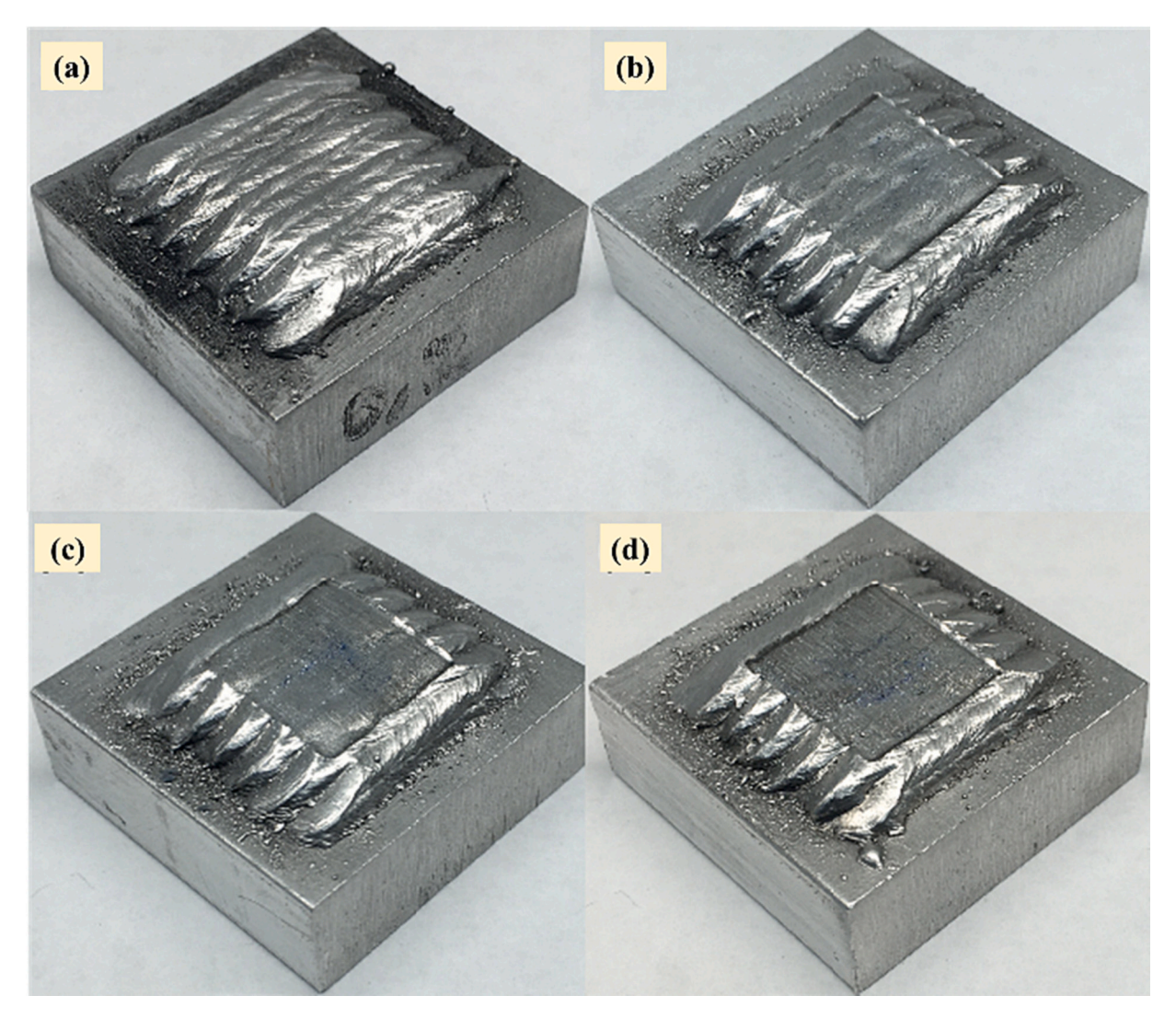


Fig. 4. Illustrating surface roughness and profile of the four WAAMed Al5356 samples with three of them surface treated with UNSM process involving (a) as-built condition, (b) UNSM 50 N case, (c) UNSM 80 N case, (d) UNSM 100 N case.

Due to this, the 3D printed texture where the influence of hatch spacing, the visibility of the area of the valley, overlapping region, tracks, depths, and depressions of the wave-like surface was no longer visible in the UNSM treated region. Except, only the 50 N UNSM case sample saw similar WAAM textures.

3. Results

3.1. Porosity studied based on the $\mu\text{-CT}$ observation

The WAAM Al5356 samples in as-built condition and UNSM-treated condition were statistically analyzed for porosity. The μ -CT scanning parameters considered for scanning are given in Table 3. The μ -CT data

Table 3 μ -CT scanning of the as-built and WAAM-UNSM-treated Al samples.

Parameters	Values		
X-ray detector size	24' × 24'		
Source-to-object distance	85.276 mm 772.7959 mm		
Source-to-detector distance			
Voxel resolution	$22.155 \mu \text{m}$		
Number of projection	720		
Tube voltage	185 kV		
Filament current	62 μΑ		

was obtained from X-ray micro-computed tomography setup as shown in Fig. 5. The scanned region includes the UNSM treated region, AM printed region, and substrate region. The reconstructed volumetric images were visualized and statistically analyzed using ORS Dragonfly software [44] for the porosity size, volume, and sphericity. In the software, a resolution of approximately $50\mu m$ was achieved to capture the smallest porosity size possible. Any porosity less than the resolution was ignored.

The average WAAM deposited layer height in the as-built condition is \sim 4.6 mm. From μ CT, it was observed that the UNSM effect on the porosity alleviation is >1.5 mm. The severe plastic deformation has eliminated most of the pores until a depth of \sim 500 μ m. Beyond the 500 μ m, up to a depth of \sim 2 mm, the micro-pores (<100 μ m) got eliminated and some of them got converted into medium pores ($<400 \ \mu m$), and the bigger pores (>400 μ m) got reduced to medium pores. From Fig. 6(a3), it was observed that in the as-built sample, due to deposited layer overlapping and the hatch spacing in the printing have caused an uneven surface profile. The pores were more concentrated along these hatch-spacing lines as shown in Fig. 6(a2). Fig. 6(b2, c2, d2) highlights the reduced sphericity of the pores. The quantity of pores and their size is shown in Fig. 6(a1, b1, c1, d1). The number of pores with a diameter of $\sim 200 \, \mu \text{m}$ which represents most of the pores in the WAAM as-built sample saw a significant decrease upon increasing UNSM static load during the surface treatment. Similarly, the number of pores with a



Fig. 5. Nikon C1 system X-ray micro-computed tomography setup used for porosity measurement.

diameter of $\sim400~\mu m$ also saw significant reduction or elimination during the UNSM treatment. It was observed that in the UNSM static load 50 N case, the large pores (> 400 μm) have been reduced to smaller size pores and was mostly eliminated upon increasing the static load from 50 N to 100 N.

Fig. 7 visually demonstrates the distribution of the individual pores in the as-built and UNSM-treated samples. It depicts the relation between the pore size and the shape of the pore through sphericity. The sphericity of 1 represents a perfect sphere and 0 represents flat geometry. To distinguish between individual pores, each pore is color coded and scaled to the volume of the pore as shown in Fig. 7(f1: g2). This helps in highlighting the major pores, their size, and their shape. From Fig. 7(e1, e2), the as-built sample saw more dispersed bigger pores of size > 1 mm. These bigger pores have a sphericity of > 0.5 representing a spherical shape in their formation. The 50 N UNSM case saw an immediate reduction of these pores and was eliminated in the 100 N UNSM sample. However, the 100 N UNSM case saw bigger pores with <0.2 sphericity. From the μ -CT, these pores were observed near the substrate where there was minimal effect of the UNSM. From Fig. 7(f2), the porosity distribution in the as-built sample saw bigger pores in the deposited region. There are >15 pores that have a volume bigger than 0.3 mm^3 . >90 % of the rest of the pores have a volume of <0.15 mm³. Because of these bigger pores, the as-built sample saw a larger pore volume range of 0.659 mm³. To analyze the porosity data, these bigger pores are considered regular pores even though it behaves like outliers that should have been omitted from consideration.

In comparison, the 50 N UNSM case saw a bigger pore with a maximum volume of $<0.25\ \text{mm}^3$ which is less than half of the maximum volume of the as-built sample. The 50 N UNSM case saw a pore volume range of 0.264 mm³. It has <10 pores that have a volume between 0.15 mm³ and 0.25 mm³. Moreover, the bigger pores in the as-built sample saw >95 % of them with a sphericity of >0.65 whereas, in the 50N UNSM static load case, >90 % of the bigger pores have a sphericity <0.5. Further, from the porosity data of the 50 N UNSM case, >90 % of the rest of the pores have <0.05 mm³ volume. That means, in between 0.05 mm^3 and 0.15mm^3 volume range, there are now only fewer than 13 pores compared to a larger number in the as-built case. These bigger pores with a volume of $> 0.13 \ \text{mm}^3$ were eliminated in the 80 N and 100 N UNSM cases. In comparison with the 50 N UNSM case, the 80 N and 100 N UNSM cases saw a maximum volume of 0.125 mm³ with a range of 0.15 mm³ and 0.135 mm³ respectively. However, compared to the 50 N UNSM case, these cases saw a greater number of pores with a volume between 0.05mm³ and 0.125mm³. Furthermore, the 100 N UNSM case saw these bigger pores with lower sphericity and lesser pore size compared to the 80 N UNSM case.

Based on these distributions of pores, with their standard deviation and mean values, the coefficient of variation (cv) for pore size, volume, and sphericity was tabulated in Table 4. As noted before in the as-built case, the outliers in the data are not omitted in analyzing for the porosity as bigger pores are important and the focus of this research. The cv highlights the influence of the UNSM on the porosity distribution in the WAAM Al5356 samples.

In the pore volume data, the drastic reduction in the cv between the as-built and the UNSM-treated samples represents less dispersion in the porosity data due to outliers. As-built samples saw more outliers with bigger pores whereas 100 N UNSM static load case saw a significant reduction in the cv. In the pore size, the 50 N UNSM case saw an increase in cv compared to the as-built case whereas the 80 N and 100 N cases saw a reduction in cv with an exponential distribution pattern. Furthermore, the cv in the sphericity represents more of a normal distribution in the data between as-built and UNSM test cases even though the UNSM test case has a slightly lower cv compared to the 100 N UNSM case.

The number of pores is based on their size, and the distribution of these pores is a subjective structure. It depends on the number of class intervals to which the sample range was considered. The individual pores visualization in Fig. 7 provides the relationship between the pore size and its class of variables such as sphericity or volume. However, it does not provide accurate information on the nature of the distribution of pores in the samples. Hence, to better understand the porosity distribution, the probability density function based on individual locations of all the pores sample data was considered using Kernel density estimation (KDE). Fig. 8 represents the non-parametric density function that uses the Gaussian function as a kernel with a bandwidth factor of 1 for univariate and bivariate density plots. The area under the curve provides the probability of the individual pores being located based on their size, volume, and sphericity.

From the univariate KDE Fig. 8(h1), it was observed that the central tendency of the pore size for the 50 N UNSM case was $\sim\!40~\mu\mathrm{m}$ that has shifted to the left of the as-built which was around $\sim\!95~\mu\mathrm{m}$. Similarly, the central tendency of the pore size for the 80 N UNSM case was $\sim\!110~\mu\mathrm{m}$, and for 100 N was $\sim\!130~\mu\mathrm{m}$ which is to the right side of the as-built case. Compared to the as-built, the 50 N UNSM case has a significant overlap with the as-built case. From the bivariate KDE plot in Fig. 8(h2), this overlap was seen in the region of pore size $<\!50~\mu\mathrm{m}$ with sphericity between 0.95 and 1.0. Continuing further, in Fig. 8(i1), the as-built sample exhibits a bimodality in the sphericity, with one peak at $\sim\!0.92$ and another higher peak at $\sim\!0.98$. Compared to this, the 50 N UNSM case also saw a bimodality in the peaks however the greater peak is at $\sim\!0.92$. This means the sphericity of the UNSM cases was on a decreasing trend with an increase in the UNSM influence. Further, the 80 N and 100

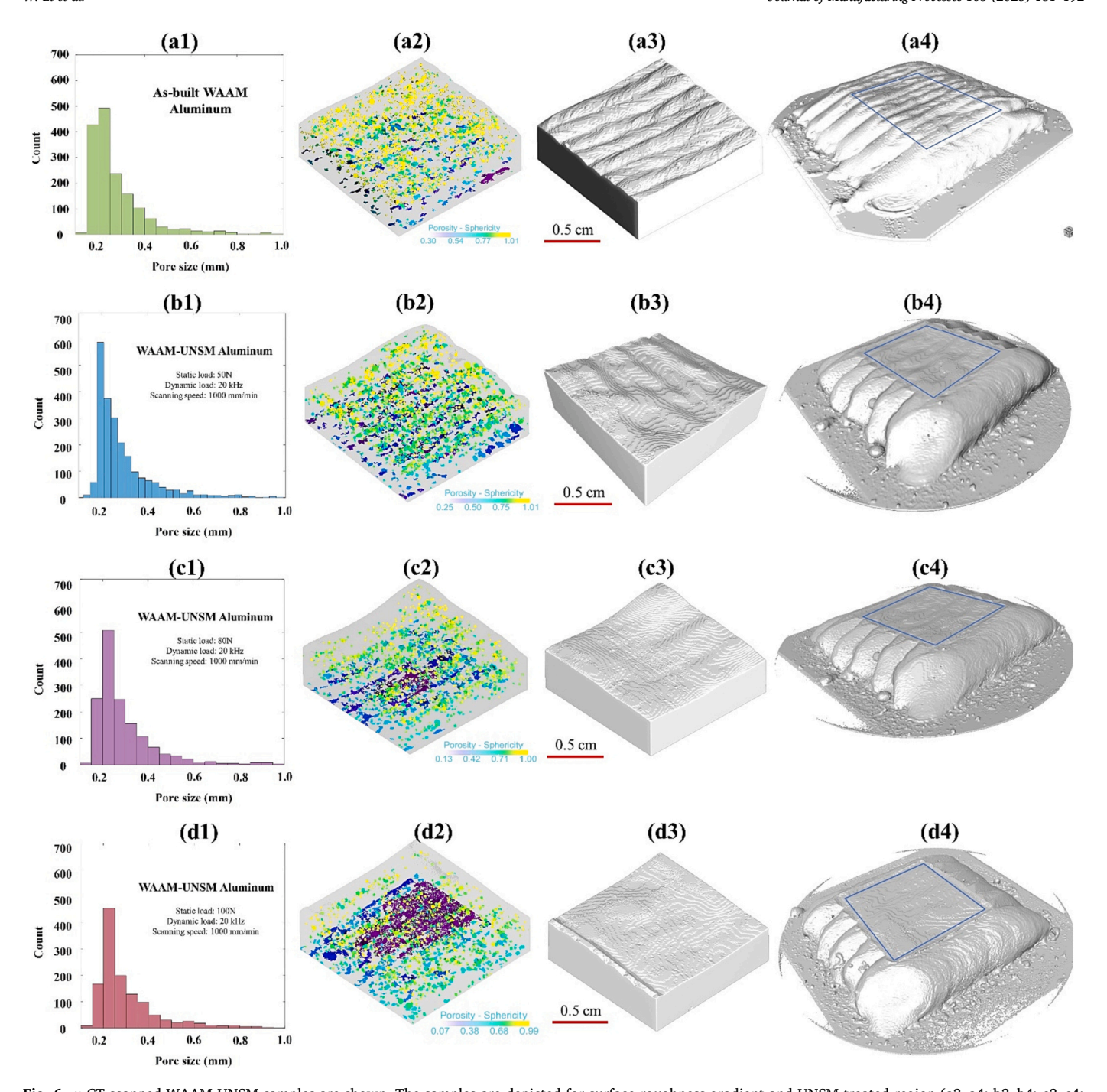


Fig. 6. μ-CT scanned WAAM-UNSM samples are shown. The samples are depicted for surface roughness gradient and UNSM-treated region (a3–a4; b3–b4; c3–c4; d3–d4), and porosity in the UNSM-treated region (a2, b2, c2, d2), and the porosity distribution in the local region selected for UNSM treatment (a1, b1, c1, d1) are shown. Row a# (a1–a4) represents the untreated as-built WAAM Al sample. Row b# (b1–b4) represents UNSM treated with a static load of 50 N as-built WAAM Al sample. Row c# (c1–c4) represents UNSM treated with a static load of 100 N as-built WAAM Al sample.

N UNSM cases saw a wider sphericity range which produced a lesser probability density of these pores. This was also observed in the bivariate KDE of the 80 N UNSM case in Fig. 8(i2) where there is a spread in the range of the pore size compared. Furthermore, the volume KDE plot in Fig. 8(j1) saw a linear distribution among all cases. However, the 100 N UNSM case saw the most non-overlapping region with the as-built case. Even though, the pore size and the sphericity spread in Fig. 8(j2) were like the 80 N UNSM case, due to pores outliers, bigger pores near the substrate region where there is minimal effect of UNSM have skewed the data.

3.2. Porosity studied based on the optical microscope observation

In order to clearly study the pore morphology under the treatments of WAAM-UNSM processes, optical microscope observations were conducted in this paper.

As shown in Fig. 9a and b, the aluminum samples were sectioned with wire electronic discharge machining following the middle cross-section. After that, rectangular specimens were cut from the middle cross-section for studying the pore morphology. Series of experimental operations were carried out to prepare the specimens for the optical

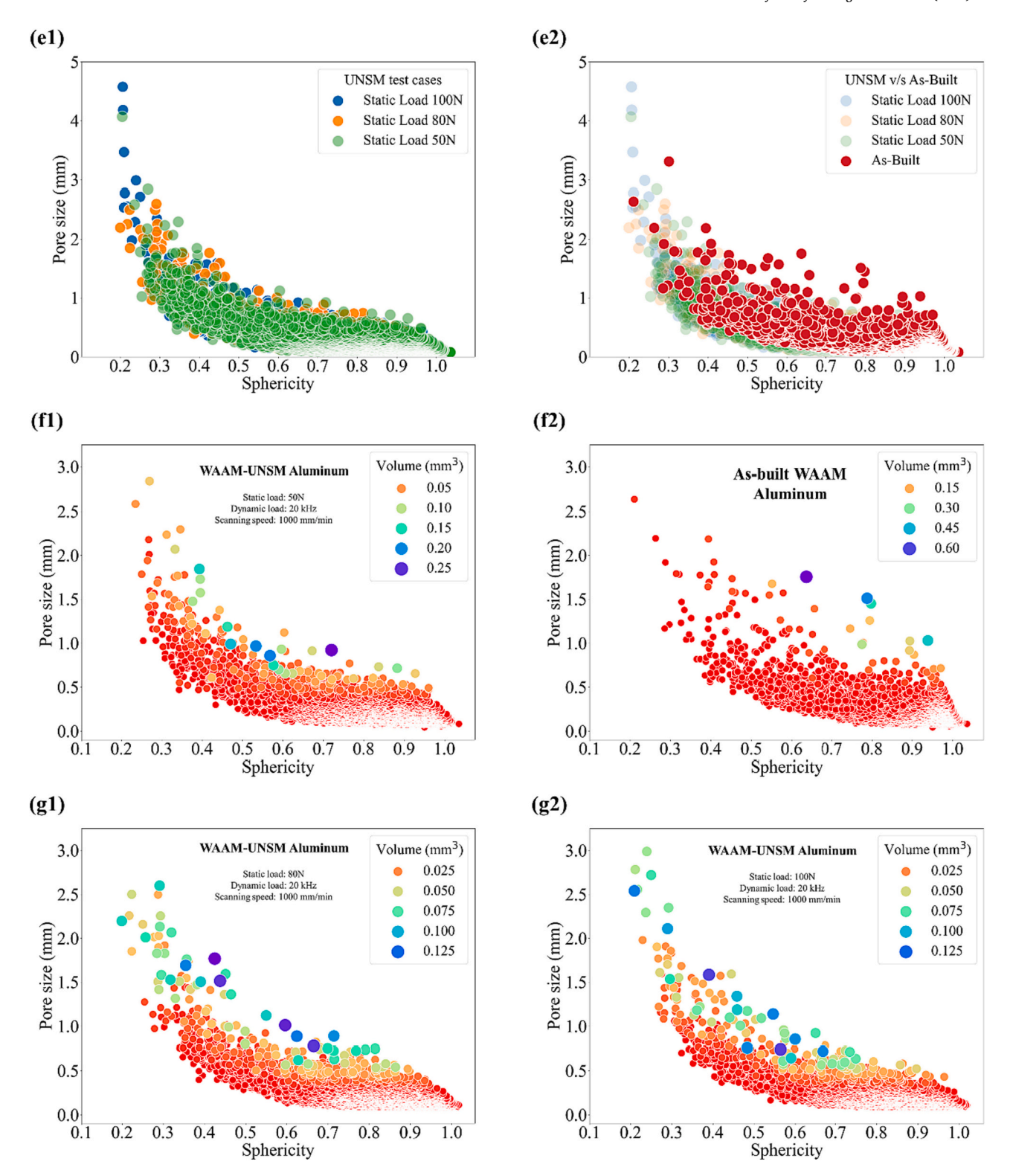


Fig. 7. A relationship between the porosity size, volume, and sphericity distribution comparison between the untreated WAAM Al sample and the WAAM-UNSM treated Al samples. (e1): WAAM-UNSM-treated Al sample cases. (e2): As-built Al sample in comparison with UNSM cases. (f2): As-built WAAM sample (f1): UNSM static load of 50 N. (g1): UNSM static load of 80 N. (g2): UNSM static load of 100 N.

microscope observation. The four rectangular specimens were mounted into the epoxy resin, then grinded with the sand papers from 600 grit to 800 grit, to 1200 grit. The grinded specimens were then polished to further smooth the surface.

Fig. 9c shows the pores morphology in the WAAMed specimen. Almost all the pores have spherical shapes with various diameters and $\frac{1}{2}$

have discrete distribution. Since the WAAM pores are mainly caused by the hydrogen vaporized from the moisture, grease, hydrocarbon contaminants on the wire surface, and the entrapped shielding gas which cannot escape due to the rapid solidification in the WAAM process, the spherical pores are the regular pore formation during the WAAM process. Fig. 9d shows the pores morphology in the WAAM-UNSM treated

Table 4The tabulated coefficient of variation based on the standard deviation and the mean values of individual pores in as-built and UNSM-treated WAAM Al5356 samples.

Test case	cv – pore size	cv – volume	cv – sphericity
As-built	0.887	8.209	0.075
50 N	0.969	7.53	0.08
80 N	0.69	3.65	0.131
100 N	0.68	3.53	0.135

specimen. The static load in the UNSM process was 50 N. One important difference is, some pores started to be merged (as shown in the yellow highlighted regions in Fig. 9d) due to the treatment of UNSM process. Fig. 9e shows the pores morphology in the WAAM-UNSM treated specimen. The static load in the UNSM process was 80 N. With the increase of UNSM static load, the WAAMed material was further compressed. Due to the plastic deformation in the UNSM process, a larger number of pores are compressed and closed by the compacting effect. Therefore, it can be clearly observed that the spherical pores were transformed into oval pores in the UNSM treated region. Fig. 9f shows the pores morphology in the WAAM-UNSM treated specimen. The static load in the UNSM process was 100 N. The increase of static load can further enhance the compacting effect in the UNSM process. In the optical microscope observation, it can be found that there is no wide spread of large spherical pores in the UNSMed region. A lot of pores were closed thus the porosity was decreased. The remaining pores are shown as oval shapes thanks to the severe plastic deformation during the UNSM treatment. Another interesting finding in the Fig. 9f is, some remaining pores had the triangle-similar shapes with sharp corner. These pore morphology results from the enhanced plastic deformation in the UNSM with highest static load 100 N.

3.3. Surface roughness

Surface roughness can affect the performance and functionality of a material or component. For example, surface roughness can affect the friction, wear, and lubrication properties of WAAMed components. A smooth surface can reduce friction and wear, while a rough surface may provide better grip or adhesion. Thus, by controlling and measuring surface roughness, it is possible to improve the reliability and quality of WAAMed components in many industries.

In this study, the center line average height (R_a) was chosen as the parameter to be evaluated. R_a is the arithmetic mean of the absolute values of the profile height deviations from the mean line, measured over the evaluation length. Specifically, the surface roughness R_a in each gradient section was assessed using a portable roughness tester (RUGOSURF 20, TESA TECHNOLOGY). Before the measurement, a calibration block was utilized to calibrate the tester, thereby ensuring more accurate test results. R_a measurements were taken ten times in each region of material composition, and all the results were recorded and used to generate boxplots as shown in Fig. 10.

The effect of UNSM on the surface roughness saw a greater smoothness in the surface profile compared to the as-built sample. Upon increasing the static load, the surface finish has improved from an average $10.4\,\mu\text{m}$ to $2.34\,\mu\text{m}$. This surface smoothness has also resulted in a reduction of micropores near the surface and a reduction in microcracks. Furthermore, this improved surface smoothness could potentially reduce the stress concentrations on the surface that could serve as crack initiation sites.

3.4. Hardness

Surface hardness is an important property of materials that can affect their performance and functionality in many engineering and manufacturing applications. Materials with high surface hardness are generally more resistant to wear and abrasion than softer materials. This is because hard materials are less likely to deform or be damaged by friction or impact. Besides, surface hardness can also affect the fatigue resistance of materials, which is important in applications where components are subjected to cyclic loading. Generally, harder materials are more resistant to fatigue failure than softer materials.

To better investigate the performance of UNSM on surface modification of WAAM samples, surface hardness is supposed to be measured and analyzed. Vickers hardness is selected as the hardness factor to be measured because it is a commonly used method to measure the hardness of materials. First, the surfaces of the UNSM samples were cleaned and flattened. Then, a square-based diamond pyramid indenter with an included angle of 136° is selected for the test. To ensure accuracy, the measurements of surface hardness were repeated several times, and took the average of the results so the error bars were made and added to the results of hardness shown in Fig. 11.

From Fig. 11, it was found that the increase in static loads saw a significant increase of >105% in the surface hardness. Such an increase in hardness can be attributed to work-hardening effects due to severe plastic deformations. Furthermore, the change in porosity distribution has contributed to the increase in hardness.

4. Conclusion

In this study, four Al5356 samples were 3D printed for single layer 12 tracks with a hatch spacing of 2 mm using a wire arc additive manufacturing process. These samples were subjected to a destructive surface modification called an ultrasonic nanocrystal surface modification. The UNSM process has induced severe plastic deformation at an ultrasonic frequency of 20 kHz, a scanning speed of 1000 mm/min, and three static load cases of 50 N, 80 N, and 100 N. The as-built and the UNSM-treated samples are characterized for porosity, surface roughness, and hardness to study the influence of UNSM treatment.

The as-built WAAMed sample saw $\sim\!2$ % of the overall pores were bigger pores within the range of 400 $\mu\rm m$ to 4067 $\mu\rm m$. This range got reduced to almost half in the 50 N UNSM case that has $\sim\!0.77$ % of overall pores between 400 $\mu\rm m$ and 3307 $\mu\rm m$. Further, the 80 N UNSM case and 100 N UNSM case saw a maximum pore size of 2597 $\mu\rm m$ and 2346 $\mu\rm m$ respectively. These cases saw $\sim\!3$ % of the overall pores that were bigger than 400 $\mu\rm m$. However, most of these pores greater than 1800 $\mu\rm m$ are located towards the substrate where there is minimal effect of the UNSM treatment. This effectively means the bigger pores under the influence of UNSM saw a greater reduction in numbers and size.

Interestingly, >56 % of the overall pores in the as-built case were micro pores within the range 40 μ m to 100 μ m. Within this range, the 80 N UNSM case and 100 N UNSM case saw a significant reduction in the number of pores close to 10 % of the overall pores. This effectively means the UNSM influence on micropores caused the micro pores due to the impact of the WC tip to either be eliminated or got merged to form a medium size pores between 100 μ m and 200 μ m. Further, the as-built case saw close to 40 % of the overall pores are medium size pores within the range 100 μm to 400 μm . Under the influence of UNSM, the 50 N UNSM case saw a reduction of \sim 50 % in the medium pores. These medium pores got either eliminated or reduced and shifted into the micropores category. Further, an increase in the static load saw a contrary effect where micropores got merged to form medium pores with overall sizes lesser than the 50 N UNSM case. This effectively means the UNSM influence on the Al5356 WAAMed samples saw an elimination of bigger pores, reduction in medium size pores in the 50 N UNSM case, and merging of micropores to form a medium size pores upon increasing the static load. Overall, upon gradually increasing the static load of the UNSM treatment, the bigger pores get eliminated, and medium pores get converted into micropores, which eventually leads to the merging of the micro pores to form medium pores of lesser pore size threshold.

The UNSM treatment on the WAAMed samples also saw a significant reduction in surface roughness. Compared to the as-built, the 50 N

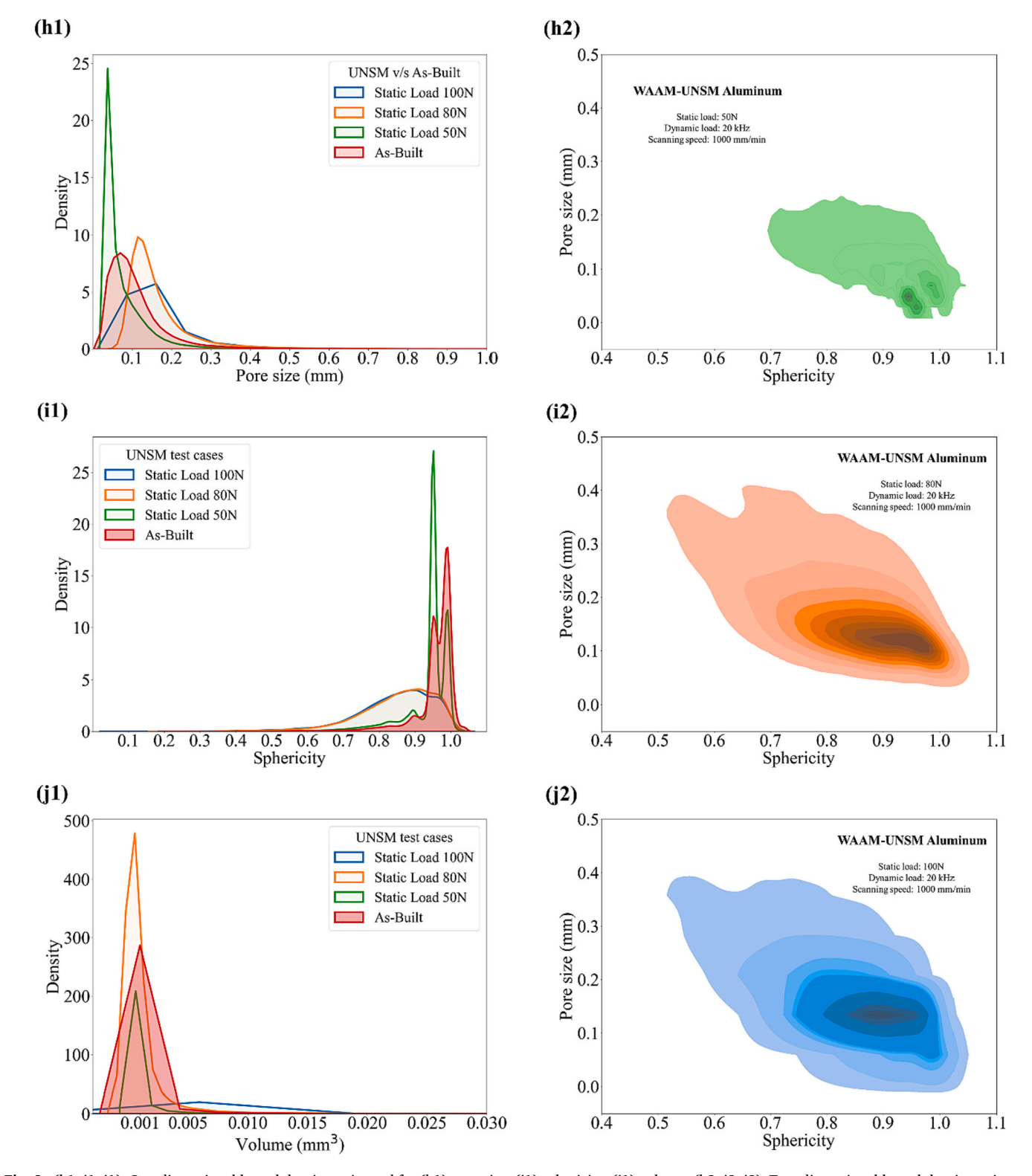


Fig. 8. (h1, i1, j1): One-dimensional kernel density estimated for (h1) pore size, (i1) sphericity, (j1) volume. (h2, i2, j2): Two-dimensional kernel density estimated distribution of pore size and sphericity for individual WAAM-UNSM-treated sample cases: (h2) UNSM static load 50 N, (i2) UNSM static load 80 N, (j2) UNSM static load 100 N.

UNSM case saw a decrease in surface roughness by $\sim\!200$ %. Further, upon increasing the static load, this lower surface roughness was both sustained and improved. Compared to the 50 N UNSM case, this surface roughness due to 80 N static load and 100 N static load saw a decrease of $\sim\!13$ % and $\sim\!23$ % respectively. This effectively means the UNSM treatment significantly reduces the surface roughness and it improved

upon increasing the static load. Overall, the cumulative effect of the reduction in porosity and its evolution, and the reduction and improvement of the surface roughness due to UNSM treatment was seen in the increase of surface hardness by $\sim\!100$ %. Thus, through a series of experiments, the excellent surface modification performance of UNSM on the WAAM Al5356 samples that saw significant changes in its shape

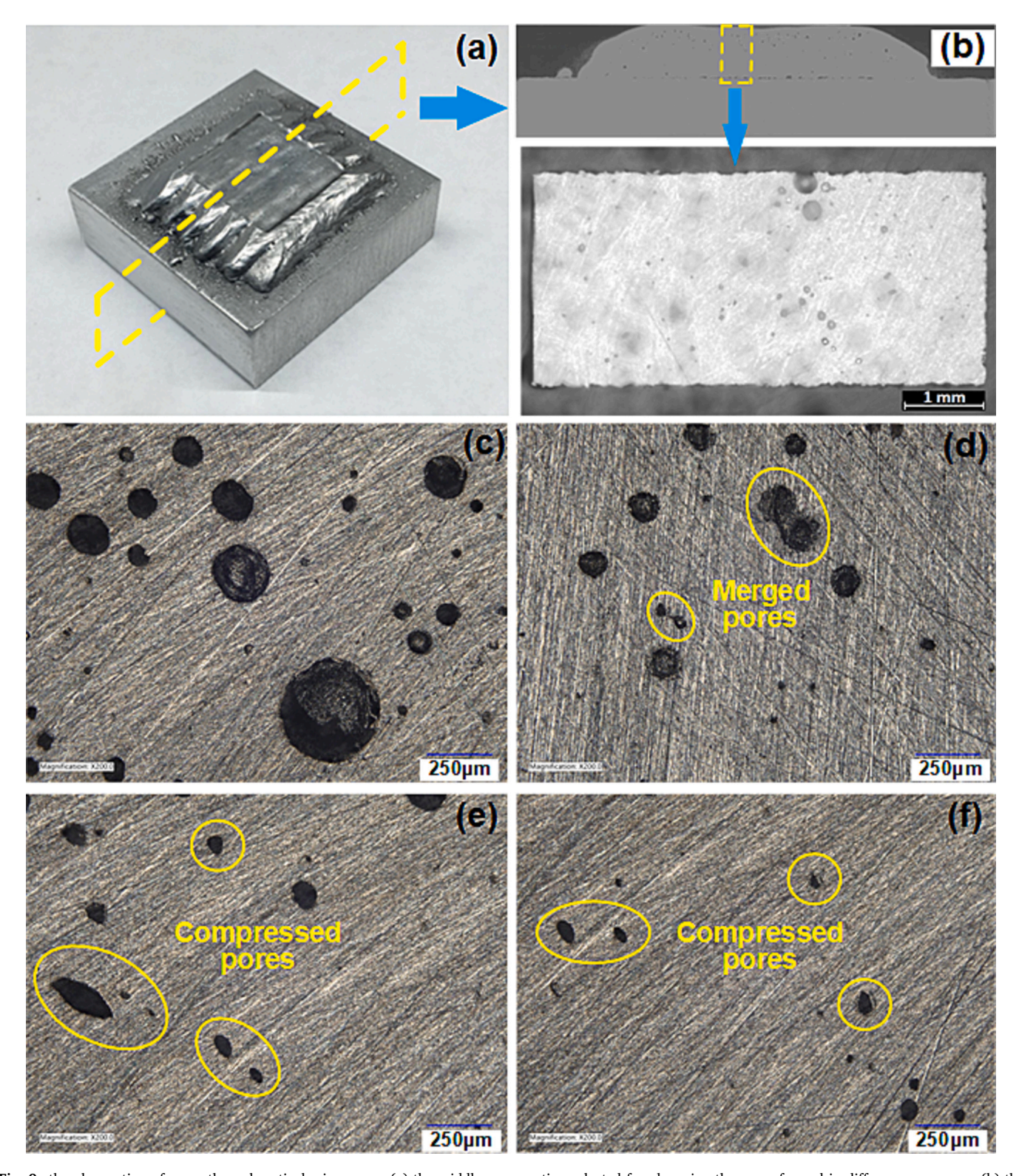


Fig. 9. the observation of pores through optical microscope, (a) the middle cross-section selected for observing the pores formed in difference processes; (b) the observation specimen cut from the middle cross-section using wire electric discharge machining; (c): pores shape and distribution in the WAAMed specimen; the shape of pores are clearly spherical; (d) pores morphology in the WAAM-UNSM specimen with UNSM static load 50 N, the pore merging can be observed; (e) pores morphology in the WAAM-UNSM specimen with UNSM static load 80 N, the oval pore shapes were obviously found in the specimen due to the compression of UNSM process; (f) pores morphology in the WAAM-UNSM specimen with UNSM static load 100 N, it can be clearly observed that the compressed pores had oval shape and smaller size.

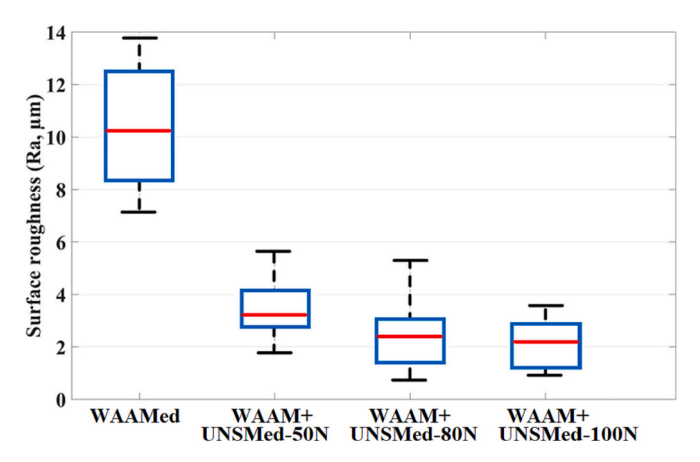
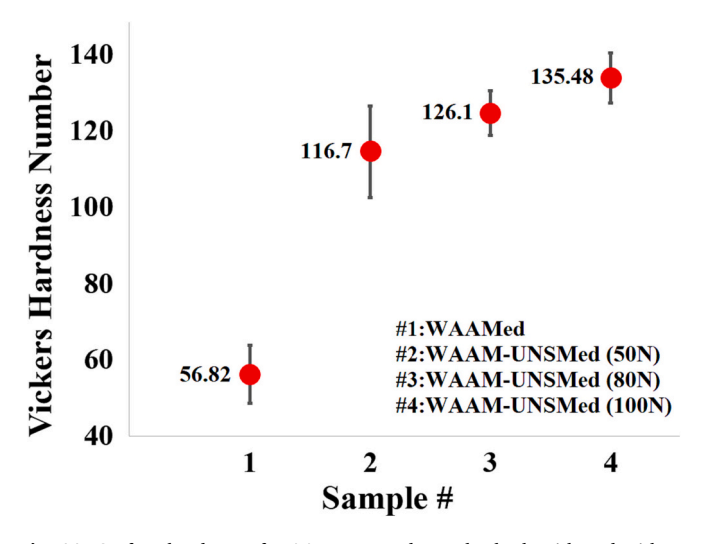


Fig. 10. The surface roughness of WAAM-prepared samples both with and without UNSM treatments.



 $\textbf{Fig. 11.} \ \ \textbf{Surface hardness of WAAM-prepared samples both with and without } \\ \textbf{UNSM treatments.}$

and form internally and externally was characterized and analyzed in this research.

CRediT authorship contribution statement

Wei Li: Conceptualization, methodology, investigation, data curation, writing, resources, supervision, project administration.

Auezhan Amanov: Methodology, data curation, writing, visualization.

Kishore Mysore Nagaraja: Conceptualization, methodology, formal analysis, investigation, data curation, writing, visualization.

Benquan Li: Methodology, data curation, writing, visualization.

Runyu Zhang: Methodology, data curation, writing, visualization. **Bharath Bhushan Ravichander:** Experiment (microscope observation) and data curation.

Golden Kumar: Resources, experiment (microscope observation). **Hongbing Lu:** Resources, methodology.

Young Sik Pyun: Resources, methodology.

Dong Qian: Conceptualization, resources, supervision, project administration.

Declaration of competing interest

The authors declare that they have no known competing financial

interests or personal relationships that could have appeared to influence the work reported in this paper.

Data availability

The raw/processed data required to reproduce these findings can be provided upon request.

Acknowledgments

The authors acknowledge the support from Sun Moon University (South Korea) in accessing the UNSM device and material characterization works. This research was partially financially supported by the Ministry of Trade, Industry and Energy (MOTIE) and the Korea Institute for Advancement of Technology (KIAT) through the International Cooperative R&D Program (P0022403). Authors R. Zhang and H. Lu acknowledge the support of NSF 2219347, and the Department of Energy under DE-NA0003962 and DE-NA0003525.

Appendix A. Supplementary data

Supplementary data to this article can be found online at https://doi.org/10.1016/j.jmapro.2023.08.047.

References

- Hauser T, Reisch RT, Breese PP, Lutz BS, Pantano M, Nalam Y, et al. Porosity in wire arc additive manufacturing of aluminium alloys. Addit Manuf 2021:41. https://doi.org/10.1016/j.addma.2021.101993.
- [2] Zhang R, Li W, Jiao Y, Paniagua C, Ren Y, Lu H. Porosity evolution under increasing tension in wire-arc additively manufactured aluminum using in-situ micro-computed tomography and convolutional neural network. Scr Mater 2023: 225 https://doi.org/10.1016/j.scriptamat.2022.115172
- [3] Babamiri BB, Indeck J, Demeneghi G, Cuadra J, Hazeli K. Quantification of porosity and microstructure and their effect on quasi-static and dynamic behavior of additively manufactured Inconel 718. Addit Manuf 2020:34. https://doi.org/ 10.1016/j.addma.2020.101380.
- [4] Maskery I, Aboulkhair NT, Corfield MR, Tuck C, Clare AT, Leach RK, et al. Quantification and characterisation of porosity in selectively laser melted Al-Si10-Mg using X-ray computed tomography. Mater Charact 2016;111:193–204. https://doi.org/10.1016/j.matchar.2015.12.001
- [5] Fu R, Tang S, Lu J, Cui Y, Li Z, Zhang H, et al. Hot-wire arc additive manufacturing of aluminum alloy with reduced porosity and high deposition rate. Mater Des 2021: 199. https://doi.org/10.1016/j.matdes.2020.109370.
- [6] Amanov A, Karimbaev R, Li C, Wahab MA. Effect of surface modification technology on mechanical properties and dry fretting wear behavior of Inconel 718 alloy fabricated by laser powder-based direct energy deposition. Surf Coat Technol 2023:454. https://doi.org/10.1016/j.surfcoat.2022.129175.
- [7] Arana M, Ukar E, Rodriguez I, Iturrioz A, Alvarez P. Strategies to reduce porosity in Al-Mg WAAM parts and their impact on mechanical properties. Metals (Basel) 2021:11. https://doi.org/10.3390/met11030524.
- [8] Arana M, Ukar E, Rodriguez I, Aguilar D, Álvarez P. Influence of deposition strategy and heat treatment on mechanical properties and microstructure of 2319 aluminium WAAM components. Mater Des 2022:221. https://doi.org/10.1016/j. matdes 2022 110974
- [9] Guo Y, Han Q, Hu J, Yang X, Mao P, Wang J, et al. Comparative study on wire-arc additive manufacturing and conventional casting of Al–Si alloys: porosity, microstructure and mechanical property. Acta Metall Sin (Eng Lett) 2022;35: 475–85. https://doi.org/10.1007/s40195-021-01314-1.
- [10] Wang F, Williams S, Colegrove P, Antonysamy AA. Microstructure and mechanical properties of wire and arc additive manufactured Ti-6Al-4V. Metall Mater Trans A Phys Metall Mater Sci 2013;44:968–77. https://doi.org/10.1007/s11661-012-1444-6.
- [11] Xue C, Zhang Y, Mao P, Liu C, Guo Y, Qian F, et al. Improving mechanical properties of wire arc additively manufactured AA2196 Al–Li alloy by controlling solidification defects. Addit Manuf 2021:43. https://doi.org/10.1016/j. addma.2021.102019.
- [12] Wang J, Zhu K, Zhang W, Zhu X, Lu X. Microstructural and defect evolution during WAAM resulting in mechanical property differences for AA5356 component. J Mater Res Technol 2023;22:982–96. https://doi.org/10.1016/j. imt 2022.11.116
- [13] Wang D, Lu J, Tang S, Yu L, Fan H, Ji L, et al. Reducing porosity and refining grains for arc additive manufacturing aluminum alloy by adjusting arc pulse frequency and current. Materials 2018;11. https://doi.org/10.3390/ma11081344.
- [14] Gu J, Ding J, Williams SW, Gu H, Ma P, Zhai Y. The effect of inter-layer cold working and post-deposition heat treatment on porosity in additively manufactured aluminum alloys. J Mater Process Technol 2016;230:26–34. https:// doi.org/10.1016/j.jmatprotec.2015.11.006.

- [15] Mclean N, Bermingham MJ, Colegrove P, Sales A, Soro N, Ng CH, et al. Effect of hot isostatic pressing and heat treatments on porosity of wire arc additive manufactured Al 2319. J Mater Process Technol 2022:310. https://doi.org/ 10.1016/j.jmatprotec.2022.117769.
- [16] Maleki E, Bagherifard S, Bandini M, Guagliano M. Surface post-treatments for metal additive manufacturing: progress, challenges, and opportunities. Addit Manuf 2021:37. https://doi.org/10.1016/j.addma.2020.101619.
- [17] Li B, Zhang R, Malik A, Li W. Machinability of partition milling stainless steel/ Inconel functionally gradient material printed with directed energy deposition. Int J Adv Manuf Technol 2022;122:3009–22. https://doi.org/10.1007/s00170-022-10111-8.
- [18] Bidulský R, Petroušek P, Bidulská J, Hudák R, Živčák J, Actis Grande M. Porosity quantification of additive manufactured Ti6AL4V and COCrW alloys produced by L-PBF. Arch Metall Mater 2022;67:83–9. https://doi.org/10.24425/ amm.2022.137475.
- [19] Li Y, Lu Y, Al Amin A, Liu WK. Stochastic Additive Manufacturing Simulation: From Experiment to Surface Roughness and Porosity Prediction. 2022.
- [20] Ge J, Pillay S, Ning H. Post-process treatments for additive-manufactured metallic structures: a comprehensive review. J Mater Eng Perform 2023. https://doi.org/ 10.1007/s11665-023-08051-9.
- [21] Ye C, Zhang C, Zhao J, Dong Y. Effects of post-processing on the surface finish, porosity, residual stresses, and fatigue performance of additive manufactured metals: a review. J Mater Eng Perform 2021;30:6407–25. https://doi.org/10.1007/s11665-021-06021-7.
- [22] Kishore A, John M, Ralls AM, Jose SA, Kuruveri UB, Menezes PL. Ultrasonic nanocrystal surface modification: processes, characterization, properties, and applications. Nanomaterials 2022:12. https://doi.org/10.3390/nano12091415.
- [23] Karimbaev RM, Cho IS, Pyun YS, Amanov A. Effect of ultrasonic nanocrystal surface modification treatment at room and high temperatures on the highfrequency fatigue behavior of Inconel 718 fabricated by laser metal deposition. Metals (Basel) 2022:12. https://doi.org/10.3390/met12030515.
- [24] Suh CM, Song GH, Suh MS, Pyoun YS. Fatigue and mechanical characteristics of nano-structured tool steel by ultrasonic cold forging technology. Mater Sci Eng A 2007;443:101–6. https://doi.org/10.1016/j.msea.2006.08.066.
- [25] Nagaraja KM, Li W, Qian D, Vasudevan V, Pyun Y, Lu H. Multiphysics modeling of in situ integration of directed energy deposition with ultrasonic nanocrystal surface modification. Int J Adv Manuf Technol 2022;120:5299–310. https://doi.org/ 10.1007/s00170-022-09082-7.
- [26] Jo YK, Gil YW, Shim DS, Pyun YS, Park SH. Control of local hardness gradient of metal surface by inclined surface treatment using ultrasonic nanocrystal surface modification. Int J Precis Eng Manuf Green Technol 2021;8:533–46. https://doi. org/10.1007/s40684-020-00303-6.
- [27] Ma C, Dong Y, Ye C. Improving SURFACE FINISH of 3D-printed metals by ultrasonic nanocrystal surface modification. In: Procedia CIRP. vol. 45. Elsevier B. V.: 2016. p. 319–22. https://doi.org/10.1016/j.procir.2016.02.339.
- [28] Lesyk DA, Martinez S, Mordyuk BN, Dzhemelinskyi VV, Lamikiz Prokopenko GI. Post-processing of the Inconel 718 alloy parts fabricated by selective laser melting: effects of mechanical surface treatments on surface topography, porosity, hardness and residual stress. Surf Coat Technol 2020;381. https://doi.org/10.1016/j. surfcoat 2019 125136
- [29] Maleki E, Unal O, Bandini M, Guagliano M, Bagherifard S. Individual and synergistic effects of thermal and mechanical surface post-treatments on wear and corrosion behavior of laser powder bed fusion AlSi10Mg. J Mater Process Technol 2022:302. https://doi.org/10.1016/j.jmatprotec.2021.117479.

- [30] Maleki E, Bagherifard S, Unal O, Sabouri F, Bandini M, Guagliano M. Effects of different mechanical and chemical surface post-treatments on mechanical and surface properties of as-built laser powder bed fusion AlSi10Mg. Surf Coat Technol 2022;439. https://doi.org/10.1016/j.surfcoat.2022.128391.
- [31] Zhang H, Zhao J, Liu J, Qin H, Ren Z, Doll GL, et al. The effects of electricallyassisted ultrasonic nanocrystal surface modification on 3D-printed Ti-6Al-4V alloy. Addit Manuf 2018;22:60–8. https://doi.org/10.1016/j.addma.2018.04.035.
- [32] Khan MA, Winowlin JT, Editors J. Innovations in Additive Manufacturing Springer Tracts in Additive Manufacturing. n.d.
- [33] Yang B, Tan C, Zhao Y, Wu L, Chen B, Song X, et al. Influence of ultrasonic peening on microstructure and surface performance of laser-arc hybrid welded 5A06 aluminum alloy joint. J Mater Res Technol 2020;9:9576–87. https://doi.org/ 10.1016/j.jmrt.2020.06.057.
- [34] Thompson A, Maskery I, Leach RK. X-ray computed tomography for additive manufacturing: a review. Meas Sci Technol 2016:27. https://doi.org/10.1088/ 0957-0233/27/7/072001
- [35] du Plessis A, Sperling P, Beerlink A, Tshabalala L, Hoosain S, Mathe N, et al. Standard method for microCT-based additive manufacturing quality control 1: porosity analysis. MethodsX 2018;5:1102–10. https://doi.org/10.1016/j. mex.2018.09.005.
- [36] Wu B, Pan Z, Ding D, Cuiuri D, Li H, Xu J, et al. A review of the wire arc additive manufacturing of metals: properties, defects and quality improvement. J Manuf Process 2018;35:127–39. https://doi.org/10.1016/j.jmapro.2018.08.001.
- [37] Efe Y, Karademir I, Husem F, Maleki E, Karimbaev R, Amanov A, et al. Enhancement in microstructural and mechanical performance of AA7075 aluminum alloy via severe shot peening and ultrasonic nanocrystal surface modification. Appl Surf Sci 2020:528. https://doi.org/10.1016/j. apsusc.2020.146922.
- [38] Ahmad Ibrahim MF, Bakar SRS, Jalar A, Othman NK, Sharif J, Daud AR, et al. Effect of porosity on tensile behaviour of WELDED AA6061-T6 aluminium alloy. Appl Mech Mater 2011;66–68:534–9. https://doi.org/10.4028/www.scientific.net/AMM.66-68.534.
- [39] McAndrew AR, Alvarez Rosales M, Colegrove PA, Hönnige JR, Ho A, Fayolle R, et al. Interpass rolling of Ti-6Al-4V wire + arc additively manufactured features for microstructural refinement. Addit Manuf 2018;21:340-9. https://doi.org/10.1016/j.addma.2018.03.006.
- [40] Ryan EM. On wire and arc additive manufacture of aluminium. University of Surrey; 2018.
- [41] Ma C, Andani MT, Qin H, Moghaddam NS, Ibrahim H, Jahadakbar A, et al. Improving surface finish and wear resistance of additive manufactured nickeltitanium by ultrasonic nano-crystal surface modification. J Mater Process Technol 2017;249:433-40. https://doi.org/10.1016/j.jmatprotec.2017.06.038.
- [42] Kim MS, Park SH, Pyun YS, Shim DS. Optimization of ultrasonic nanocrystal surface modification for surface quality improvement of directed energy deposited stainless steel 316L. J Mater Res Technol 2020;9:15102–22. https://doi.org/ 10.1016/j.jmrt.2020.10.092.
- [43] Bai L, Jiang K, Gao L. The influence and mechanism of residual stress on the corrosion behavior of welded structures. Mater Res 2018:21. https://doi.org/ 10.1590/1980-5373-MR-2018-01660.
- [44] Object Research Systems. Dragonfly 2020.2. Montreal, Canada: Object Research Systems (ORS) Inc; 2020. software available at, http://www.theobjects.com/ dragonfly (Computer software, n.d.).